PHYSICAL REVIEW MATERIALS **5**, 044601 (2021)

Influence of surface band bending on a narrow band gap semiconductor: Tunneling atomic force studies of graphite with Bernal and rhombohedral stacking orders

Regina Ariskina,[1] Michael Schnedler,[2,*] Pablo D. Esquinazi,[1,†] Ana Champi,[3] Markus Stiller,[1] Wolfram Hergert,[4]
R. E. Dunin-Borkowski,[2] Philipp Ebert,[2] Tom Venus,[5] and Irina Estrela-Lopis[5]
[1]*Division of Superconductivity and Magnetism, Felix-Bloch Institute for Solid State Physics, University of Leipzig, D-04103 Leipzig, Germany*
[2]*Peter Gruenberg Institut, Forschungszentrum Juelich, D-52425 Juelich, Germany*
[3]*Centro de Ciencias Naturais e Humanas, Universidade Federal do ABS, Santo Andre, 09210-580 SP, Brazil*
[4]*Institute of Physics, Martin Luther University Halle-Wittenberg. D-06120 Halle, Germany*
[5]*Institute of Medical Physics and Biophysics, University of Leipzig, D-04107 Leipzig, Germany*

(Received 21 January 2021; accepted 22 March 2021; published 5 April 2021)

Tunneling atomic force microscopy (TUNA) was used at ambient conditions to measure the current-voltage (I-V) characteristics at clean surfaces of highly oriented graphite samples with Bernal and rhombohedral stacking orders. The characteristic curves measured on Bernal-stacked graphite surfaces can be understood with an ordinary self-consistent semiconductor modeling and quantum mechanical tunneling current derivations. We show that the absence of a voltage region without measurable current in the I-V spectra is not a proof of the lack of an energy band gap. It can be induced by a surface band bending due to a finite contact potential between tip and sample surface. Taking this into account in the model, we succeed to obtain a quantitative agreement between simulated and measured tunnel spectra for band gaps (12 . . . 37) meV, in agreement with those extracted from the exponential temperature decrease of the longitudinal resistance measured in graphite samples with Bernal stacking order. In contrast, the surface of relatively thick graphite samples with rhombohedral stacking reveals the existence of a maximum in the first derivative dI/dV, a behavior compatible with the existence of a flat band. The characteristics of this maximum are comparable to those obtained at low temperatures with similar techniques.

DOI: 10.1103/PhysRevMaterials.5.044601

I. INTRODUCTION

Is ideal graphite, a carbon-based structure composed by weakly coupled graphene layers, a semimetal or a narrow-gap semiconductor? This fundamental question and the possibility of a spontaneous symmetry breaking [1] that may trigger a narrow energy gap was not clarified in earlier experiments. The main reason is that most of the earlier experimental studies were done using samples with a considerable amount of highly conducting stacking faults (SF) parallel to the graphene planes of the graphite structure [2]. The dominant stacking order of the graphene layers is the Bernal (2H) stacking order (ABABA...). There is also a minority phase, called rhombohedral (3R) (ABCABCA...), occurring with a concentration $\lesssim 25\%$ in bulk samples [3–5]. Hence, well ordered graphite samples contain SF being two-dimensional (2D) interfaces between twisted 2H, twisted 3R regions, or between the 2H and 3R stacking orders. Several reports in the last 12 years on the internal structure of well ordered, pyrolytic as well as natural graphite samples characterized by transmission electron microscopy (TEM) and x-ray diffraction (XRD), revealed a significant amount of SF separated by a few tens to several hundreds of nm in the c-axis direction [2,5–10]. These 2D SF show quite different electronic properties, which dominate the conductance at certain temperature and magnetic field ranges of high quality, highly ordered graphite samples [11,12].

Scanning tunneling microscopy (STM) measurements done on well ordered graphite or bilayer graphene samples at room and low temperatures indicate that those SF can be also found at or very near the sample surface [13–15] altering the density of states (DOS) locally [16]. Kelvin force microscopy studies of the surface of well-oriented graphite samples, done in air as well as in inert atmosphere, revealed the coexistence of insulating- and conductinglike regions [17], whose origin can also be related to the presence of ideal graphite and regions with SF at or near the surface, respectively. These highly conducting 2D SF are the origin for the metalliclike behavior in the temperature dependence of the resistance [2,11], for the low temperature Shubnikov-de Haas and de Haas-van Alphen quantum oscillations [10,11] and also for the huge diamagnetism of graphite [18] at fields applied parallel to the c axis [19]. In other words, the proposed Fermi surface [3] does not correspond to ideal graphite, in contradiction to the semimetal picture proposed more than 60 years ago [20–22]. Finally, some of the SF are at the origin of the observed granular superconducting behavior of graphite: Whereas twisted graphene bilayers show superconductivity at $T < 10$ K [23] (related to the existence of a flat band [24]), higher critical temperatures have been reported earlier due to internal and larger SF in bulk and TEM lamellae [7–9,25], partially containing the 3R phase [5,26].

The experimental facts that speak for a semiconducting nature of ideal graphite are the following.

---

[*] m.schnedler@fz-juelich.de

[†] esquin@physik.uni-leipzig.de

a. Longitudinal electrical resistance. Thin graphite samples with a low or negligible amount of SF show an exponential temperature dependence in the electrical resistance compatible with a semiconducting behavior [2] with an energy gap in the order of ~30 ± 10 meV for the 2H phase and ~110 ± 15 meV for the 3R phase [27]. The small band gaps of the 2H or 3R phases combined with the huge electrical anisotropy of graphite, as well as the contribution of the 2D SF to the total conductance of a sample [2], can be anticipated to be at the origin of the complex, even contradictory temperature and magnetic field dependences of the transport properties found in literature [10,11]. An exponential decay with temperature of the longitudinal resistance can be taken as a semiconducting fingerprint that challenges the usual semimetal description of the band structure of ideal graphite, assumed in the past on the basis of the McClure, Slonczewski, and Weiss calculations [20–22].

b. Magnetoresistance. Indirect support for the semiconducting behavior of graphite is given by the magnetic field dependence of the magnetoresistance at temperatures T above 50 K and fields to 65 T. In these ranges, the contribution of the SF to the magnetoresistance turns out to be negligible in comparison to that of the graphene matrix [12,28]. The field dependence of the magnetoresistance can be well understood within a two-band model indicating the existence of an energy gap between a valence and a conduction band [28].

c. Hall effect. A further example of the influence of defects in graphite samples is the sign of the Hall coefficient. Out of thirteen published studies on the Hall coefficient of different graphite samples (not few-layers graphene) [29–41], nine reported positive Hall coefficient at a certain field and temperature range [29–36,41]. The differences in the Hall coefficient have been partially explained by taking into account SF within the graphite matrix [41]. Graphite appears to be another example of solids for which both, intrinsic and extrinsic effects contribute to the Hall coefficient, making a direct estimate of the intrinsic carrier densities difficult [41].

d. Optical spectroscopy. Optical pump-probe spectroscopy with 7-fs pump pulses indicates that at ultrafast time scale graphite does not behave as a semimetal but as a semiconductor [42].

Regarding studies on graphite with the two different stacking orders using angle-resolved photoemission spectroscopy (ARPES) we would like to mention the following recent publications. A gaplike feature of 25 meV between the π and $\pi^\star$ bands at the K(H) point was reported [43], whereas in Ref. [44] an energy gap of 37 meV was inferred from the band fits near the H point. A gaplike feature at an energy of $\simeq$67 meV was reported in Ref. [45] and interpreted as a phonon-induced gap. Recently, similar results were obtained by ARPES in combination with scanning tunneling microscopy/spectroscopy (STM/STS) studies in highly oriented pyrolytic graphite (HOPG) of, however, unreported quality [46]. Very similar dI/dV characteristics curves with clear gaplike features were obtained by STS, independently of the used tip material (Ag, Pt/Ir, or W), prior to exposing the sample to hydrogen molecules [46]. This similarity is actually not expected because of the large differences between the contact potentials of the used tip materials and graphite, a fact that affects the I-V characteristics, as we will see below. Improvements in the ARPES technique allow measurements with a resolution of $\lesssim$100 nm in the sample surface plane. This is a necessary resolution because of the lack of large single crystalline regions in usual graphite samples [47]. We note, however, that the usual energy resolution of $\gtrsim$5 meV appears still not enough to clearly resolve a semiconducting energy gap of the order of 30 meV. Nano-ARPES measurements on a long sequence of 3R stacking order showed the existence of a flat band, where 25 meV dispersion appears to be compatible with a magnetic ground state characterized by an energy band gap close to 40 meV [48].

The aim of this work is to unravel whether tunneling atomic force spectroscopy can provide further evidence for the semiconducting nature of graphite and whether differences can be measured at room temperature between the two stacking order phases. We used a relatively new tunneling spectroscopy technique, called tunneling atomic force microscopy or TUNA, and in particular the PeakForce operation mode [49]. The overall results are compatible with the interpretation that ideal graphite with 2H phase is a narrow band-gap semiconductor and that the 3R phase, found in thick flakes, exhibits a maximum in the DOS at its surface, compatible with the existence of a flat band in the electronic spectrum [48,50–52].

II. RESULTS AND DISCUSSION

All TUNA results presented in this work were obtained in air at normal conditions on natural and HOPG samples of grade A and micrometer size flakes obtained from the corresponding bulk pieces. The quality and stacking order characterization of the samples were done using Raman spectroscopy, as done in previous reports [53–56]. The I-V curves were obtained in the tunneling regime with currents between a few tens of pA to $\lesssim$3 nA. Further details about samples and characterization methods are provided in Sec. IV below.

A. Bernal stacking order

1. *Experimental tunneling spectra*

Figure 1 shows the normalized I-V characteristics and their first derivatives (see insets) for the bulk HOPG sample (a) and a graphite flake (b). Raman spectroscopy indicates that the main phase in those samples is the 2H phase. Figure 1(a) illustrates normalized I-V curves of the bulk samples, measured at three different spatial positions. All three curves are nearly identical. Analogous measurements on the thin graphite flakes reveal similar I-V curves as for the bulk sample, although with somewhat larger local variations, as depicted in Fig. 1(b). These small spatial variations of the current can be observed in general for thin graphite flakes and are not necessarily related to the presence of SF at the surface but due to bending or defective regions.

Our normalized I-V curves are asymmetric, and the first derivative of the normalized current exhibits a minimum at $V \simeq 0.12$ V, see the inset in Fig. 1(a). An early STM work on graphite at ambient conditions reported a relatively wide minimum at low voltages in the differential conductance [57]. Similar curves were obtained at 4.2 K on very thin graphene multilayer samples with the Bernal phase [50].

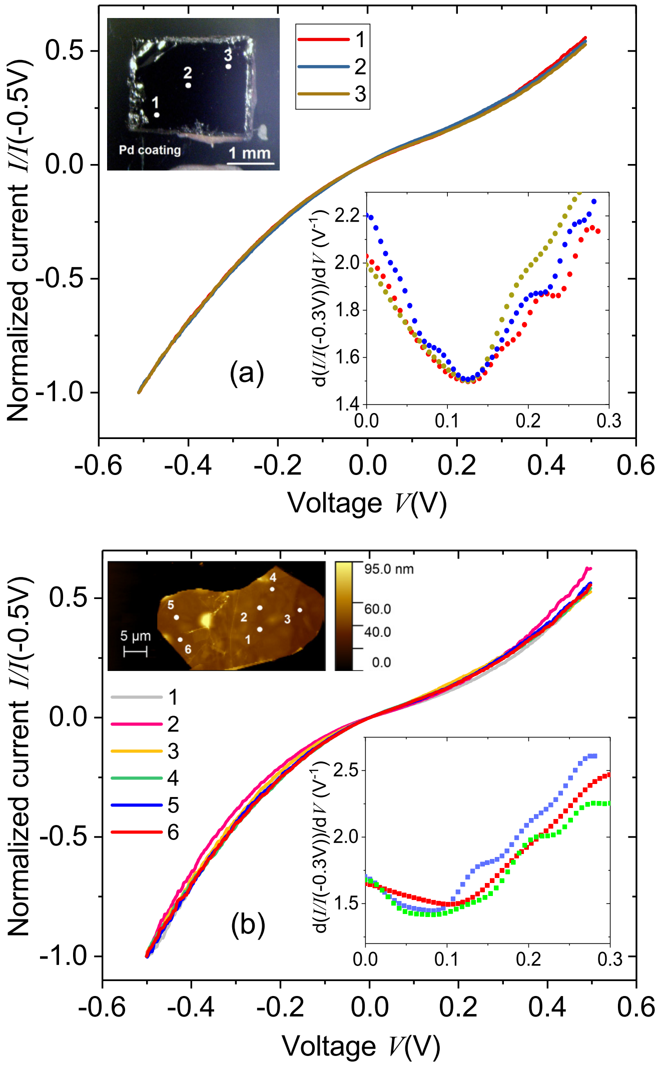

FIG. 1. (a) Normalized TUNA current-voltage characteristics measured in the tunneling regime at different positions of a HOPG sample (HOPGA-Pd-1, see Table I), see optical image in the upper left inset. The maximum current values at -0.5 V used for the normalization were first to third locations): 217 pA, 302 pA, 240 pA. The lower right inset shows the first derivative of the I-V curves at the three locations. The normalization of the current values with the first derivative was done at -0.3 V (instead of -0.5 V as in the main panel) to enhance the details in the region of interest. Figure 9 shows the first derivative in the whole measured voltage range for the same sample. (b) Similar measurements for a graphite mesoscopic flake (sample MG-Pd-11-2) (see SEM image at the upper left inset) at different positions. The maximum current values at -0.5 V used for normalization were: 1174 pA, 912 pA, 565 pA, 597 pA, 671 pA, 447 pA. The inset below right shows the first derivative of the I-V curves at three locations (current normalized at -0.3 V). All results were obtained at ambient conditions.

At first view, the normalized I-V curves in Fig. 1 exhibit apparently no band gap, i.e., a voltage region without detectable tunneling current. On the other hand, the first derivative dI/dV is a quantity generally assumed to be proportional to the LDOS. Although in a classical semiconductor model a minimum in the LDOS can be a trace of a band gap, it is not a sufficient criteria to infer its existence. The simulation of the I-V spectra proposed below can help to discern to which extent the existence of a (small) energy gap is compatible with the measured spectra.

2. *Simulation of the spectra*

In view of the aforementioned difficulties that prevent a direct observation of a band gap using the I-V curves, we turn to a different approach: First, we assume that graphite behaves like an ordinary semiconductor. Under this assumption, a software package, specifically designed for simulating tunneling currents at semiconductor surfaces [58,59], is employed to investigate the influence of the size of the band gap on the I-V curves. By comparing simulated I-V curves with those experimentally obtained on graphite with Bernal stacking, we conclude that the measured spectra can be understood using an ordinary semiconductor model by assuming small band gaps. Finally we try to estimate the size of the band gap from the TUNA measurements.

In order to derive the tunneling current, we follow the two-step method as described in Refs. [58,59]: First, we performed self-consistent electrostatic simulations of the tip-vacuum-semiconductor system to unravel the potential and carrier distributions in three dimensions. A Pt-Ir tip with a radius of 100 nm and opening angle of 45° was chosen. The carrier concentrations of the sample are derived using the parabolic band approximation (see, e.g., Ref. [60]). Band gaps ranging from 0.1 meV to 120 meV are assumed. The graphite's Fermi-level position E_F as well as the concentration of free electrons $n(E_F, T)$ and holes $p(E_F, T)$ at a temperature of $T = 300$ K are defined by solving the charge neutrality condition:

$$n(E_F, T) - p(E_F, T) + N_A(E_F, T) - N_D(E_F, T) = 0\,, \quad (1)$$

with $N_A(E_F, T)$ and $N_D(E_F, T)$ being the acceptor and donor concentrations. Several Hall effect results [29–36,41] suggest that graphite should be degenerated with a Fermi level located inside the valence band with a free carrier concentration of the order of 10^{17} cm^{-3} at 300 K [41,61]. We assume density of states effective masses of the order of one hundredth of the electron rest mass for a parabolic band approximation. Using these constraints, we can solve the charge neutrality condition only if a certain concentration of shallow acceptor states is incorporated. Due to the lack of the precise knowledge about the graphite density of states effective masses and acceptor ionization energies, it remains to be clarified in a future work, whether the assumed concentration of shallow acceptors states depends on the concentration of atomic lattice defects in our HOPG samples. Note that those defects can play a role in the effective carrier density, as irradiation studies indicate [62].

Without bias ($V = 0$), the contact potential is defined as the work function difference between the metallic probe tip (Pt_{80}-Ir_{20}) and the graphite sample. It affects the tip-induced band bending in the same manner as the application of a bias voltage. For Pt and Ir work function values between 5.7 and 5.8 eV were reported [63]. On the other hand for graphite the work function varies from 4.6 [64] to 4.7 eV [65]. Taking into account these values, the contact potential between the probe tip and graphite surface is expected to be $\simeq$1 eV.

In a second step, we use the one-dimensional electrostatic potential along the central axis through the tip apex to derive

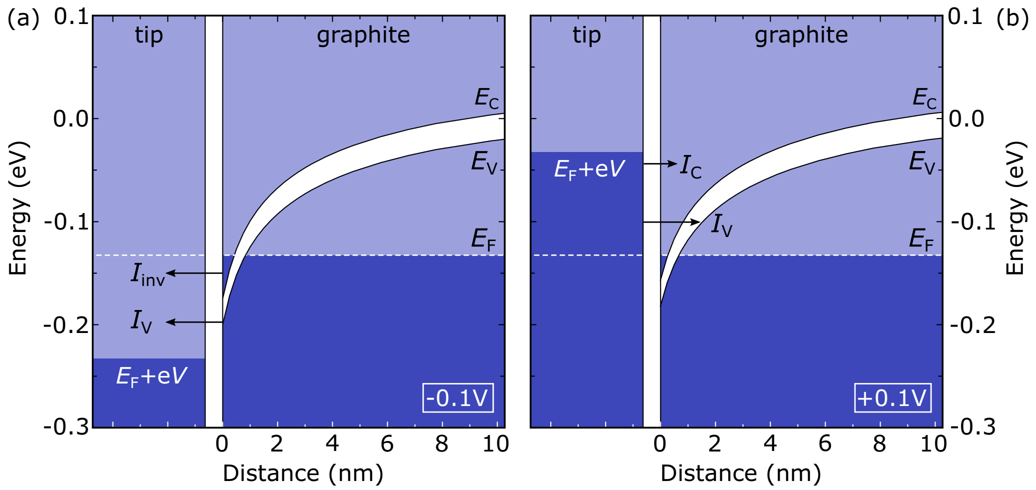

FIG. 2. Tip-induced band bending as a function of the distance from the graphite surface for a biased tip-vacuum-sample system. (a) At negative sample voltages, tunneling out of filled valence band states (I_V) is dominating the total tunneling current. In addition, due to the large downward band bending and the small band gap, the conduction band minimum is dragged below the Fermi level at the surface, filling up its states with electrons. These electrons can tunnel out of the conduction band into empty tip states, leading to an additional, but small, tunneling current component (I_{inv}). (b) The large downward band bending is also present at positive sample voltages, due to a large contact potential of $\simeq$1 eV. The total tunneling current is again composed of two components: The first component is driven by tunneling of electrons from the tip into empty valence band states (I_V). This is only possible because the Fermi level of the sample is situated below the valence band maximum, leading to unoccupied states within the valence band. The second component is driven by electrons tunneling from filled tip states into empty conduction band states (I_C). At small positive sample voltages, I_V is the dominant tunneling current component, while for large positive voltages, I_C becomes the largest contribution to the total tunneling current.

the tunneling currents through the vacuum barrier using the WKB approximation based model described in Refs. [66,67]. In order to fit the measured I-V curves to the calculated ones, we took the band gap, the effective masses, the concentration of acceptors, and the tip-sample separation as fit parameters.

3. Modeling of the tunneling current based on the tip-induced band bending

As discussed above, from experiments we expect a free carrier concentration of the order of $\sim 10^{17}$ cm^{-3} (i.e., $\sim 3 \times 10^9$ cm^{-2} per graphene layer) at 300 K for Bernal graphite. For such a carrier concentration the electrostatic potential, present between the metallic probe tip and graphite during STM experiments, cannot be screened completely at the graphite surface and can reach the subsurface region of the material (commonly referred to as tip-induced band bending). We take the tip-induced band banding into account in our self-consistent simulations.

The above discussed contact potential of $\simeq$1 eV in conjunction with small band gaps lead to empty and filled states, which are simultaneously present in *both* valence and conduction band. Hence, at negative bias (sample) voltages the tunneling out of filled valence- and conduction-band states into empty tip states occurs, while at positive voltages, tunneling from filled tip states into empty valence- and conduction-band states takes place. This situation is illustrated in Fig. 2. Even at positive sample voltages, the downward band bending remains present. In contrast to other p-type semiconductors with larger band gaps, tunneling into empty conduction band states (I_C) occurs even for very small positive sample voltages already (in addition to the tunneling current I_V into empty valence band states). At a sample voltage of approximately $\sim$+0.12 V the increasing I_C becomes larger than the decreasing I_V, leading to the above discussed minimum in the first derivative dI/dV.

A good agreement between the measured and simulated I-V curves at Bernal stacked graphite surfaces was achieved as indicated by the green solid line in Fig. 3. This simulation was obtained for a free carrier concentration of 2.3×10^{17} cm^{-3}, similar to the expected one [41,61], a band gap of 25 meV, similar to that obtained from transport results [2,27], as well as effective masses of 0.01 and 0.0075 for the valence- and conduction-band, respectively. We restricted the calculations within the voltage range of interest ±0.3 V. In the same figure we show the simulations obtained with the same parameters but for band gaps 0.1 meV and 50 meV.

In order to investigate the influence of a band gap on the tunneling spectra of graphite, we calculated I-V curves for band gaps between 0.1 meV and 120 meV. Figure 4 shows that in particular the tunneling current at the positive voltage branch decreases with increasing band gap. This behavior is caused by an interplay of two effects: First, the shift of the graphite's conduction band states towards larger energies with increasing band gap leads to less conduction band states that are available for tunneling. Second, a larger band gap leads to an energetically increased tunneling barrier between tip and sample, which in return decreases the tunneling probability. Hence, also the tunneling current related to valence band states decreases slightly with increasing band gap. This delicate interplay alters the slope of the combined tunneling current (i.e., the sum of conduction- and valence-band related tunneling currents) at positive sample voltages and defines the position of the minimum of the dI/dV curves. Larger

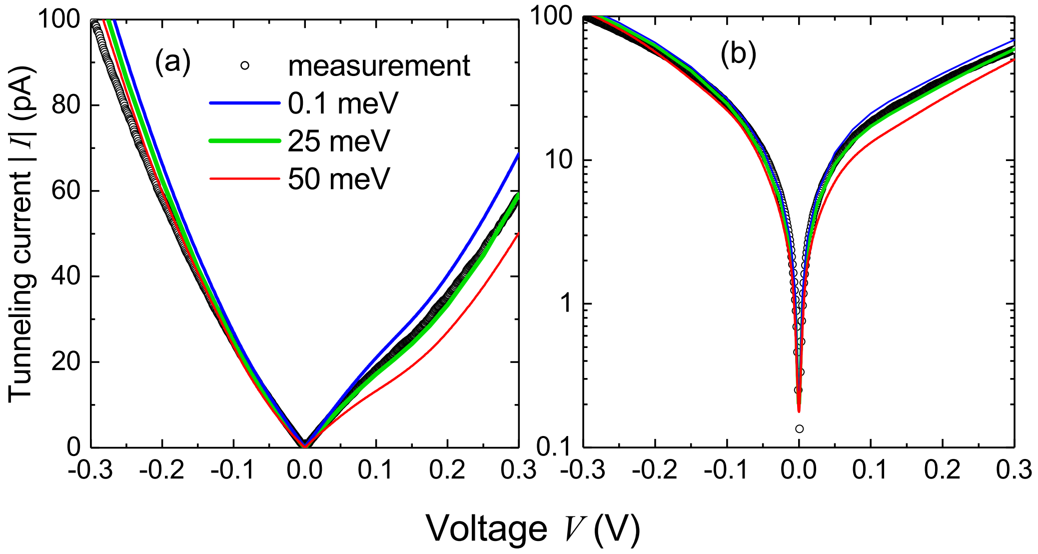

FIG. 3. Comparison of TUNA spectra measured at clean and atomically flat Bernal-stacked graphite surfaces at $T = 300$ K. The symbols correspond to the curve obtained at position 1 for the HOPG sample (HOPGA-Pd-1) shown in Fig. 1(a) with the best fit tunneling current simulation (green solid line). The blue solid line was obtained choosing a band gap of 0.1 meV with the same set of parameters, see Fig. 4. The results are plotted in a (a) linear and (b) logarithmic scale. In order to better recognize the asymmetry of the I-V curves between the positive and negative voltage ranges, we plotted the absolute values of the tunneling current values of the experimental as well as the computed currents. Note the change in the curvature of the I-V curve at $V \sim 0.12$ V and the difference in the absolute values of the current at ±0.3 V.

band gaps result in stronger curvatures at the positive voltage branch, while for small band gaps the positive voltage branch becomes more linear. In the limit of a vanishing band gap, the minimum in the dI/dV curve is still present. Note that thermal broadening of the Fermi-Dirac distribution of the $\mathrm{Pt_{80}Ir_{20}}$-tip states is not taken into account in the tunneling current computation, which can however be anticipated to not change the position of the minimum in the dI/dV curve but only its intensity.

Although the simulations with smaller and larger band gap appear to agree less with the experimental data according to the depicted graph $|I|$ vs V shown in Fig. 3, a clear distinction is difficult on this basis alone. A more sensitive way is given by comparing the first derivative and in particular the position of its minimum. The reason is that the minimum in the dI/dV curve is found to shift with the band gap as illustrated in Figs. 5(a) and 5(b). As one can recognize in this graph, the first derivative of one of the I-V curves obtained for sample HOPG-Pd-1 as example [see Fig. 1(a)] roughly agrees with the simulation with energy gap of 25 meV with a minimum at $V_{\mathrm{min}} = 0.127 \pm 0.007$ mV. We further quantified the voltage position of the experimentally observed minima by fitting a polynomial of ninth grade to the numerical differentiation of all I-V curves, yielding an average value of $V_{\mathrm{min}} = 0.122 \pm 0.005$ mV. The experimental region of the minimum is shown as the shadowed area in Fig. 5(b). The comparison of the measured V_{min} values with the simulated V_{min} vs the band gap E_G suggests that the experimental data can be described best with a semiconductor model with a band gap between 12 meV and 37 meV. From the simulated $V_{\mathrm{min}}(E_G)$, see Fig. 5(b), we note that the data obtained for the mesoscopic graphite sample with Bernal stacking order, see Fig. 1(b), suggest that larger and a broader distribution of band gaps could be localized at certain regions of the inhomogeneous or bended graphite surface. We may speculate that atomic lattice defects, other than simple SF, but twisted or turbostratic stacking with more complexes sequences may have different band gaps.

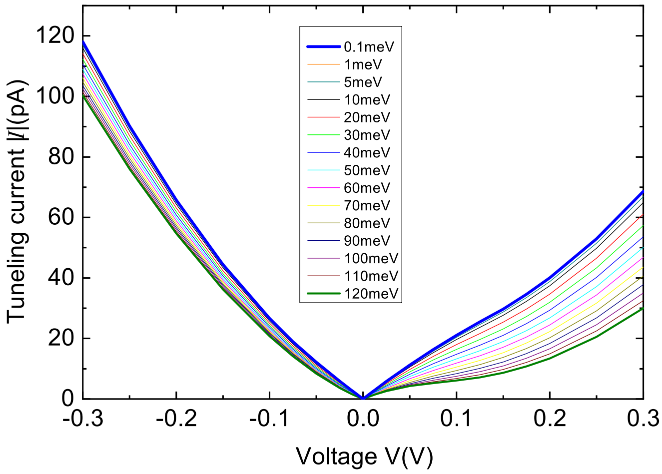

FIG. 4. Simulated tunneling current vs bias voltage at different band gaps between 0.1 meV and 120 meV using the parameters explained in the main text. Note that the absolute values of the current are plotted.

We varied the parameters of the simulations to estimate the error range. A decrease of the contact potential leads to a slight increase of the band gap (~4 meV per 0.1 eV decrease) while decreasing the free carrier concentration ($\sim 4 \times 10^{16}$ $\mathrm{cm^{-3}}$ per 0.1 eV decrease) and the effective band masses. Taking into account transport data [41,61], we expect that the carrier concentration is at least $\gtrsim 10^{17}$ $\mathrm{cm^{-3}}$ at 300 K. Hence, the contact potential should be $\gtrsim 0.7$ eV, which restricts the band gap to $\lesssim 40$ meV. Taking into account

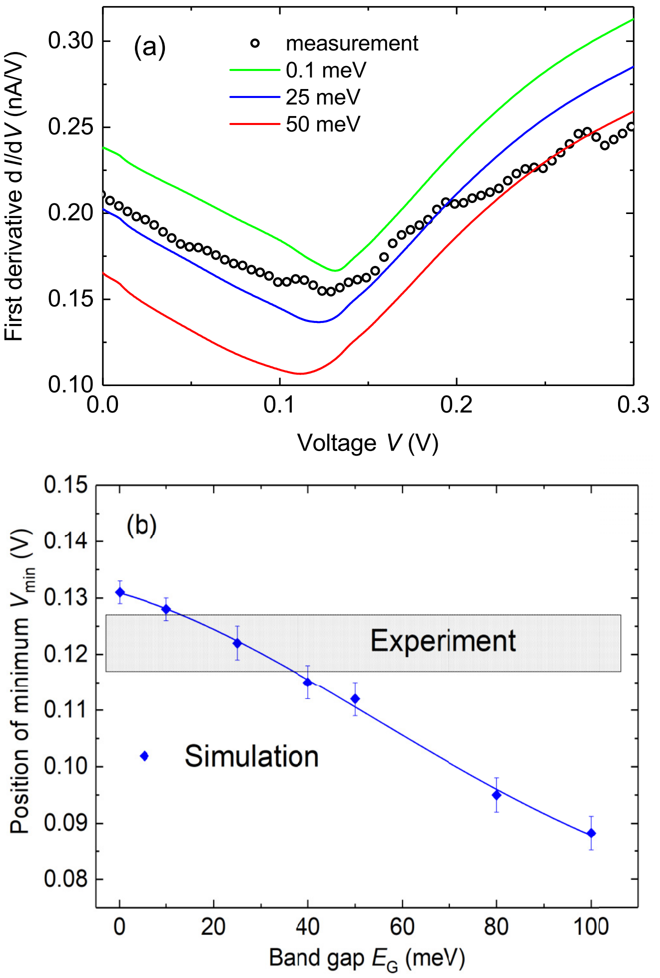

FIG. 5. (a) (○): First derivative of the tunnel current vs applied voltage measured on the HOPG-Pd-1 sample shown in Fig. 1(a) and (lines) of the simulated tunnel currents at three different band gaps (0.1, 25, 50) meV with otherwise unchanged parameters. Note that the absolute values of the derivative are plotted. (b) Voltage position of the minimum of the first derivative vs the band gap E_G. The (♦) were obtained from the simulations. The line is only a guide to the eye. The range of the minimum in the first derivative of the experimental *I*-*V* curves of the HOPG-1 sample is given by the shadowed rectangular region.

correlation effects between the parameters, we estimate an error in the carrier density parameter of $\pm 1.5 \times 10^{-17}$ cm^{-3}. We note that if we assume a negligible band gap at contact potentials smaller than 1 eV, the deviation between the measured data and the theoretical curve increases, pointing further to the existence of a finite energy gap.

We conclude this section by pointing out that the measured spectra for the Bernal stacking order are best described by a semiconductor model with a narrow band gap. In the first approximation the first derivative spectra is proportional to the LDOS, although the voltage scale is shifted by the existence of a tip-induced band bending. Taking advantage of these insights in the interpretation of the tunneling spectra on Bernal stacking order graphite, we now turn to measurements of the rhombohedral stacking order of graphite.

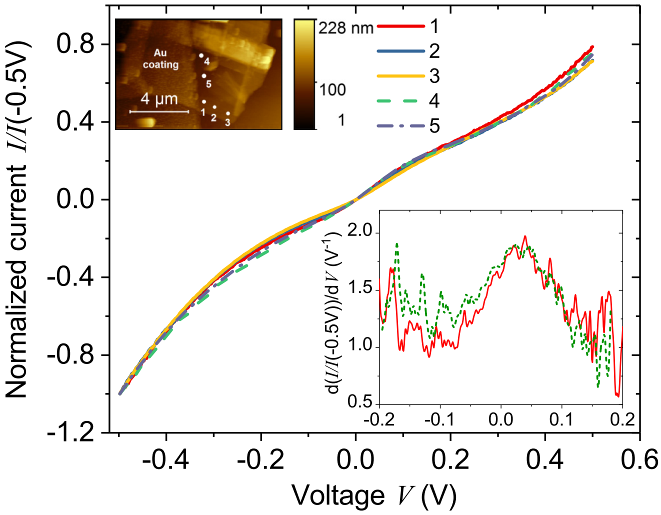

FIG. 6. TUNA current-voltage characteristics obtained at different positions of the 3R phase surface of a 22 nm thick (≃22 unit cells) natural graphite flake (sample NBF5-01-03, see Table I), see upper left inset with the AFM image. The current values used for normalization were (from first to fifth positions): 276 pA, 293 pA, 386 pA, 374 pA, 366 pA. The bottom right inset shows the first derivative of the *I*-*V* curves at the first and fourth positions in the voltage region of interest.

B. Rhombohedral stacking order

The 3R phase is of especial interest nowadays due to the expected flat band at its surface or at its interfaces with the 2H stacking order [51,68]. A flat band in the 3R phase has been found experimentally [48,50,69,70], which correlates with a maximum in the DOS at the Fermi level, enhancing the probability to trigger superconductivity [51,52,71] and/or magnetism [48,72,73] at high temperatures. In particular, STS obtained on a sequence of five layers of 3R phase showed a peak in the DOS around the Fermi level with a width of ∼50 meV at half maximum [50]. We have performed TUNA measurements in several natural graphite samples with the 3R phase. For a relatively thick (22 nm) sample with the 3R phase, we measured a clear maximum in the differential conductance reproducible at different positions spread by several μm^2 in the sample area, see Fig. 6. This maximum is not observed, however, in a 3R phase sample of much smaller thickness (3 nm), see Fig. 7. This difference may indicate that either the roughness of the samples plays a detrimental role or the number of 3R unit cells in the thin sample is not enough to clearly develop this feature at room temperature, as numerical simulations suggest [51].

We note that the maximum in the differential conductance observed in the thicker 3R sample is shifted by ∼40 meV above the zero level and with a width at half maximum of ∼100 meV. Those values are of the same order as reported at 4.2 K, in spite of ≃70 times higher temperatures, stressing the robustness of the high DOS feature around the Fermi level at the surface of this graphite phase. The shift of the maximum in the differential conductance may come from the influence of a finite contact potential and band bending.

We note that the temperature dependence of the resistance measured for a large number of bulk samples from different

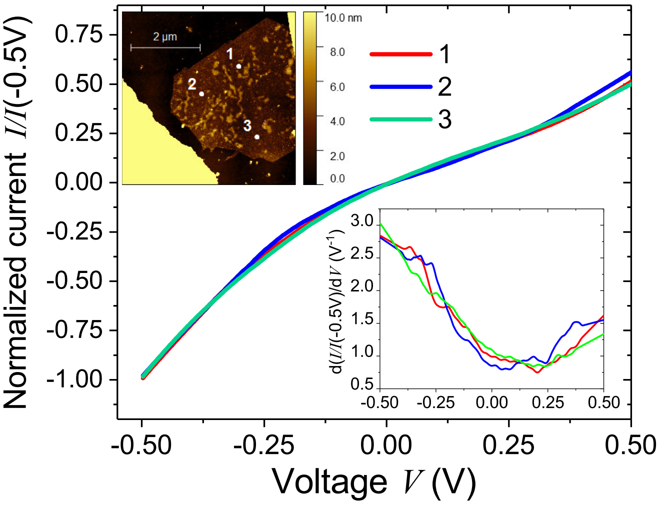

FIG. 7. TUNA current-voltage characteristics obtained at three different positions of the 3R phase surface of a 3 nm thick ($\simeq$3 unit cells) natural graphite flake (sample NBF5-SNG-3, see Table I), see upper left inset with the AFM image. The current values at -0.5 V used for the normalization were (from first to third positions): 241 pA, 222 pA, 213 pA. The bottom right inset shows the first derivative of the normalized current $I(V)$ curves.

origins follows over a very broad range ($2\ \text{K} \lesssim T \lesssim 1100\ \text{K}$), the temperature dependent resistance known for semiconductors, suggesting that this minority 3R phase should also be a narrow gap semiconductor with an energy gap of the order of 100 meV [27]. Under this assumption we would have the situation of a different band structure at the surface from that in the bulk of the 3R phase. The position of the minimum in the first derivative obtained for the thinner samples, see inset in Fig. 7, cannot be determined with sufficient accuracy because it depends very much on the spatial position on the sample. Much better sample quality of thin enough 3R phase samples is necessary to check for a semiconducting behavior with a larger energy gap than in the Bernal case as transport measurements suggest [27]. Mean field theoretical studies indicate [74] that the only possible origin for an energy gap in the bulk of the 3R phase should be related to a spontaneous symmetry breaking, a feature that needs more work to verify its existence.

III. CONCLUSION

Characteristic current-voltage curves obtained by tunneling atomic force spectroscopy (TUNA) on Bernal stacked graphite surfaces can successfully be reproduced by using classical self-consistent semiconductor modeling in conjunction with quantum mechanical tunneling current derivations, taking into account a nonzero band gap as well as reasonable values for the carrier concentration and effective masses of graphite. The best simulation could be obtained for band gaps in the range $(12\ldots37)$ meV, in agreement with previous transport and Hall-effect studies. The agreement between simulated and measured tunneling currents at 300 K should be considered as a demonstration that the assumption of graphite being a semiconductor with a narrow band gap is in line with the measured data. In particular our model explains the minimum in the dI/dV curves at $V \simeq 120$ mV. It is the result of a delicate interplay of tunnel currents arising from valence- and conduction-band states at both positive and negative sample voltages. Furthermore, we showed that the lack of a voltage region without detectable current in the I-V spectra is not sufficient to exclude the presence of a band gap. In analogy, a voltage range without detectable current is not one-to-one equal to the fundamental band gap [75,76].

In contrast to the results obtained from samples with Bernal stacking, the surface of samples with the rhombohedral stacking order indicate a clear maximum in the differential conductivity, in agreement with previous STS results obtained at much lower temperatures, suggesting the existence of a flat band at the Fermi level. On the other hand, very thin samples with rhombohedral stacking order show a minimum in the first derivative at positive voltages, whose voltage positions depend very much on the sample location.

IV. SAMPLES AND METHODS

A. Samples

The origin, thickness, and method for electrical contacts of the measured samples are given in Table I. The bulk HOPG Grade A sample, from which we prepared the samples HOPGA-Pd-1, MG-Pd-11-1, MG-Pd-11-2, and A1 (see Table I), was obtained from Advanced Ceramics (now Momentive Performance Materials). The total impurity concentration (with the exception of H) of the HOPG and natural graphite samples is below 20 ppm, see Refs. [5,77] for more details.

TABLE I. Characteristics of the measured samples. The electrical contacts of the samples (last column) were done through lithography at the sample top surface or directly on the bottom sample surface using Pd-coated substrates. 3R means rhombohedral stacking order, 2H: Bernal stacking order.

Sample	Thickness (nm)	Origin	Stacking order	Contacts
NBF5-01-03	22	Brazil mine	3R	lithography
NBF5-01-05	40	Brazil mine	mixture of 2H and 3R	lithography
NBF5-SNG-3	3	Brazil mine	3R	lithography
NBF5-01-09	8	Brazil mine	2H	lithography
HOPGA-Pd-1	300	HOPG Grade A	2H	Pd-coated
MG-Pd-11-1	65	HOPG Grade A	2H	Pd-coated
MG-Pd-11-2	40	HOPG Grade A	2H	Pd-coated
A1	45	HOPG Grade A	2H	Pd-coated

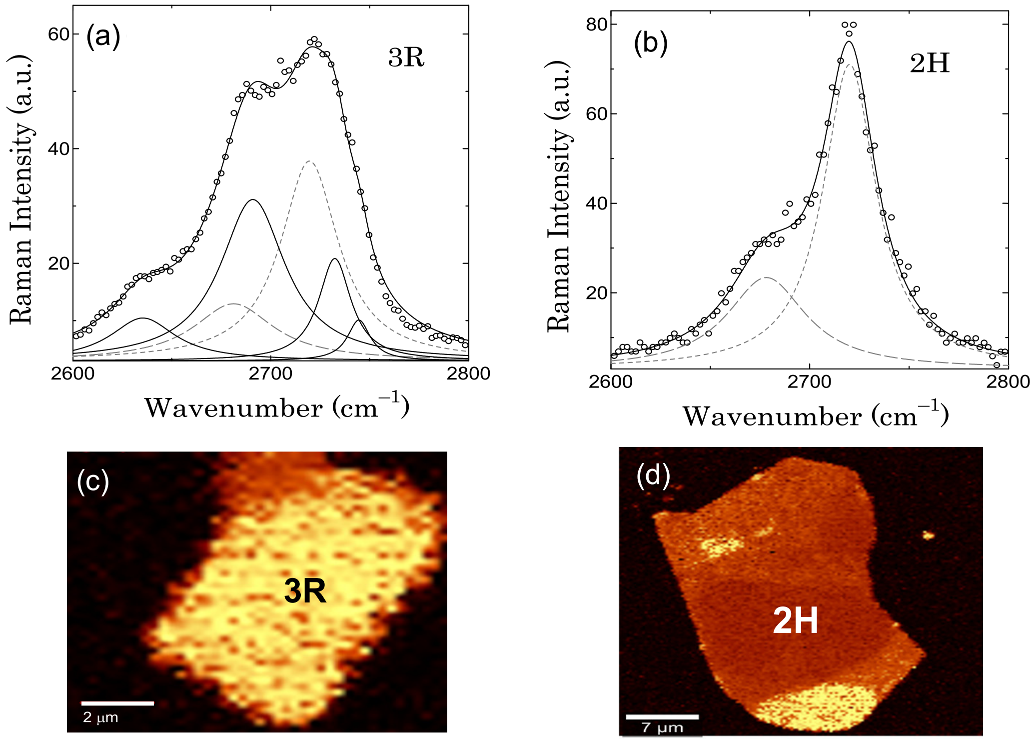

FIG. 8. (a) Average of the 2D band of the rhombohedral phase (3R) showing the six processes due to ABC stacking of the NBF5-01-03 natural graphite flake sample. (b) Average of the 2D band of the Bernal phase (2H) showing the two process due to ABA stacking of MGPd-11 HOPG flake sample. (c) Raman image of the spatial distribution of the 2D band width. The yellow color area shows the 3R phase. (d) Raman image for the spatial distribution of the 2D band. In this case the red color area represents the Bernal phase (2H).

Graphite flakes were prepared using a mechanical cleavage. The method consists of mechanically gently rubbing a bulk graphite sample onto a thoroughly cleaned in ethanol substrate. After that, the substrate with the multigraphene flakes is well cleaned in an ultrasonic bath of highly concentrated acetone for one minute several times.

Different ways of electrical contacts fabrication were applied. The investigated graphite samples were placed on top of two differently prepared silicon substrates with a 150 nm thick insulating silicon nitride (Si_3N_4) coating. On one of the two substrates we patterned electrodes on the samples top surface and on the insulating substrates using electron beam lithography followed by sputtering of a bilayer Cr/Au (5 nm/30 nm). Other graphite samples were electrically contacted by depositing their bottom surface to a 100 nm thick Pd layer sputtered on the Si_3N_4 coating (after depositing a buffer layer of 31 nm thick Cr).

B. Raman characterization

Microscopic analysis of the graphite stacking orders and sample quality were realized by Raman spectroscopy measurements. Raman spectra of multilayer graphene samples were obtained with a confocal micro-Raman microscope WITec alpha 300+ at 532 nm wavelength (green) at ambient temperature, see Fig. 8 as example. All Raman measurements were performed using a grating of 1800 grooves mm^{-1}, 100× objectives (NA 0.9), and incident laser power of 1 mW. Lateral resolution of the confocal micro-Raman microscope was ~300 nm and the depth resolution ~800 nm.

The Raman results revealed Bernal and rhombohedral stacking orders as well as a mixture of those phases depending on the sample. The areas with different stacking orders have been localized by surface scanning and registration of spectra at each point in increments of 100 nm with the confocal micro-Raman microscope. Afterwards, the function of automatic recognition of the given shapes of the spectrum curves showed the regions with different stacking.

Figures 8(a) and 8(b) present the Raman spectra in the 2D Raman bands for the rhombohedral (3R) area of the NBFG5-01 sample and Bernal (2H) area of the MGPd-11 sample. The spectra are the average obtained by hyperspectral scanning within the respective regions. Figures 8(c) and 8(d) show the Raman image that is obtained analyzing the spatial distribution of the 2D bandwidth of the NBF5-01 and MGPd-11 samples. Following recent publications [53–56] there are three main Raman scattering features in rhombohedral stacking order of the graphite structure. The main one that can be used to find the 3R phase is the absorption at the G'-band with a broad peak around $\simeq$2700 cm^{-1}, as shown in Fig. 8(a), in clear contrast to the corresponding peak measured in the 2H phase, see Fig. 8(b). According to the Raman results the investigated samples presented in this study are of high structural quality due to the absence of the disorder-related D-peak around $\simeq$1350 cm^{-1} (not shown).

These results indicate that while the smaller area in the NBF5-01 sample has a Bernal stacking order, the larger area consists of a rhombohedral one. The opposite is observed in the other sample shown in Fig. 8(d).

C. TUNA measurements

Local current-voltage (I-V) curves measurements were performed with a Bruker dimension icon scanning probe microscope equipped with PeakForce tunneling AFM module (PF-TUNA) [49]. The PeakForce tapping mode is based on a quick contact interaction of the probe and the sample (tens to hundreds of microseconds). PeakForce TUNA mode with a bandwidth of 15 kHz allows the measurement of a current averaged over the full tapping cycle. All measurements were conducted at room temperature and at ambient conditions. Pt-Ir-coated silicon nitride probes with a nominal radius of 25 nm (PF-TUNA, spring constant = 0.4 N/m, resonant frequency = 70 kHz) have been used. PeakForce tapping amplitude was set to 150 nm. A current sensitivity of 100 pA/V was used in all measurements. The bias voltage was swept from −500 mV to 500 mV on flat surface regions. In order to decrease the noise in the data, the I-V curves shown in this study were taken from an average of 25 consecutive I-V ramps at a single point.

The measurement and calibration of the I-V curves at certain parts of the selected samples were performed as follows: First the I-V curves were measured on a test sample—a floppy disk. After checking the operability, the cantilever was moved to the graphite sample and a 20 nm^2 area was scanned in order to localize the flat areas without irregularities. Then a point was chosen in an area of 5×5 nm^2 or 1×1 nm^2 to register the I-V curves. The PeakForce setpoint (trigger force) was chosen as small as possible in order not to damage the surface.

To rule out possible artifacts (e.g., when a piece of graphite sticks at the tip), to check the reproducibility of the measurements and the state of the used Pt-Ir probes, three different tests were used, namely: After each measurement the response of the Pt-Ir probe was examined using the reference sample (FD sample, 12 mm from Bruker). Furthermore, scanning electron microscope (SEM) was used to check for the state of the probes tips. In order to avoid distortion in the data, each probe was used not more than 25 h. After that we continued with a new probe. In the case of the samples with the 3R phase two different probes were used to check for the reproducibility of the unusual behavior at low voltages.

Finally, to verify that the shift of the minima in dI/dV to positive bias voltages obtained in the graphite samples is not an artifact, we selected a n-type semiconducting sample with a larger band gap than graphite but still relatively narrow. Just after measuring one sample with Bernal stacking and without changing the probe or any sets of the microscope, we measured a hydrogenated diamondlike carbon (DLC) film, the one usually used in old magnetic hard disks. Upon hydrogenation and defect concentration the energy gap of the DLC films can be as low as a few hundreds of meV. The measured I-V curve

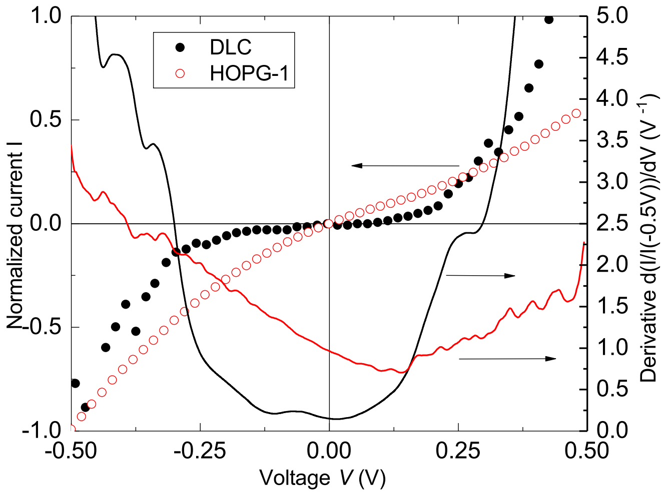

FIG. 9. TUNA results of the current-voltage characteristic curves (left y axis) and their first derivatives (right y axis) measured on a diamondlike carbon film (DLC) and on the position 1 of the bulk graphite surface of Fig. 1(a). The maximum current values used for normalization were: 59 pA (●) and 217 pA (○). The red line of the first derivative corresponds to the graphite sample and the black one to the DLC film. The derivatives were obtained from the normalized current data at −0.5 V.

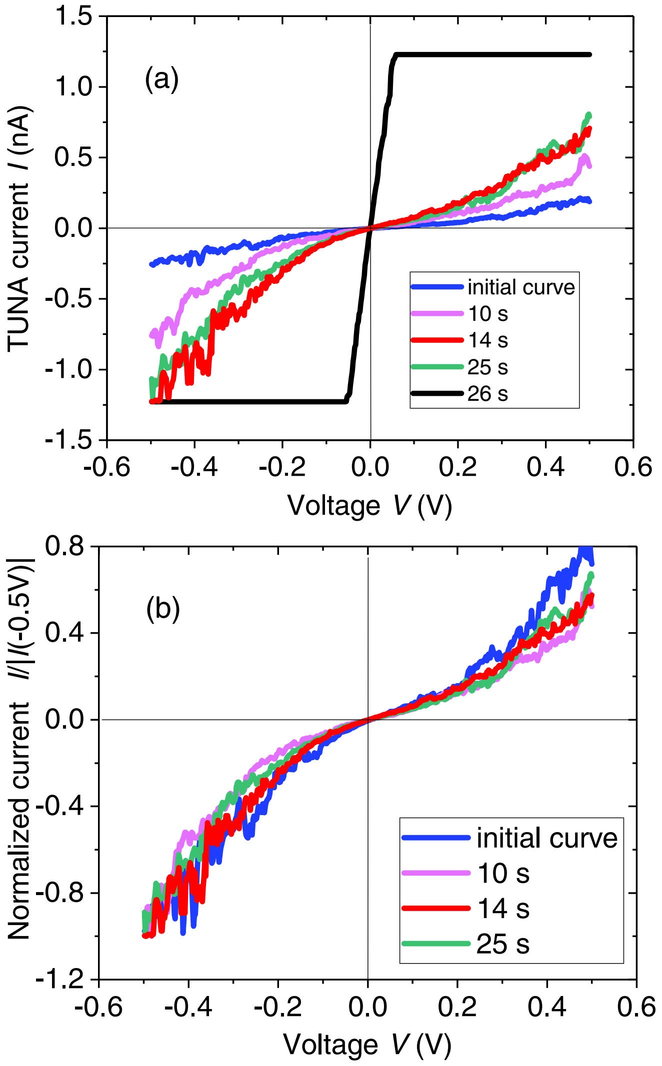

FIG. 10. (a) Single (no averaging) TUNA current vs bias voltage curves obtained on sample HOPGA-Pd-1 (2H phase) at a fixed location in the continuous ramping mode at different times. After 26 s the tunneling current saturates already at low bias voltages just before a direct contact between the tip and the sample surface occurs. (b) The same data as in (a) in the tunneling regime but normalized by their corresponding currents at −0.5 V.

of the DLC film is shown in Fig. 9 together with its differential conductance (right axis). For comparison, in the same figure we include one of the curves obtained from the bulk HOPG sample shown in Fig. 1(a). The *I-V* curve of the DLC film and its derivative indicate an energy gap $E_g \gtrsim 0.25$ eV. Note that the *I-V* curve of the DLC film shows an opposite asymmetry as for graphite, i.e., it is shifted to negative bias voltages.

The TUNA equipment allows in principle a constant current scan to get a scan image of the conductance variation across the sample surface. This useful tool cannot be easily used for graphite due to the soft *c*-axis elastic module of the graphite structure. When one uses this mode, and due to the soft elastic module, a time dependence in the *I-V* curves is observed. Measurements of the time dependence of the *I-V* spectra were carried out with the graphite sample HOPG-Pd-1 using the spectroscopy mode in the PeakForce TUNA mode. In order to obtain a series of *I-V* curves at one fixed position the continuous ramping mode was used with the parameters: 2 V set point, 100pA/V sensitivity, and ramp rate of 1.03 Hz. The cycle was repeated automatically after a certain time. Overall, 26 *I-V* curves were obtained within 26 s; some of them are shown in Fig. 10. These measurements indicate a variation of the tunneling current with time. The observed behavior is similar to the one observed from tunneling regime to point-contact changing the tip-sample distance in Ref. [57]. In the tunneling regime, i.e., at low enough current amplitudes and before a direct contact is achieved, all *I-V* curves show the same behavior after normalization, see Fig. 10(b). This effect should be taken into account when measuring electrical characteristics of soft materials with PF-TUNA mode. From the technical point of view, the obtained results indicate that the TUNA technique allows spectroscopy studies in natural and pyrolytic graphite samples. Care must be taken with time dependent effects due to the soft *c*-axis module of graphite and the setpoint selected in the TUNA electronics.

ACKNOWLEDGMENTS

The author P.D.E. thanks Tero Heikkilä, Francesco Mauri, Vladimir Volovik, Jose-Gabriel Rodrigo, Andrei Pavlov, and Eberhard K. U. Gross for fruitful discussions. We thank Laetitia Bettmann for her help during the studies. This work has been possible with the support of the European Regional Development Fund, Grant No. 231301388. A.C. acknowledges 2MI and VRS Eireli Research & Development for the financial support and Nacional do Grafite, MG (Brasil), for the samples.

R.A. carried out the TUNA measurements. R.A. and A.C. carried out the sample preparation. T.V. and I.E-L. performed the Raman measurements. A.C. and R.A. contributed to the interpretation of the Raman results. M.Sc. contributed to the interpretation of the results and performed all numerical studies. W.H., R.E.D-B., and P.E. contributed to the interpretation of the results. M.St. helped in the measurements and purchasing the microscope with all the used options. P.D.E. conceived and planned the experiments. P.D.E. and M.Sc. took the lead in writing the paper. All authors provided critical feedback and helped shape the research, analysis, and paper.

---

[1] F. Zhang, H. Min, M. Polini, and A. H. MacDonald, Phys. Rev. B **81**, 041402(R) (2010).

[2] N. García, P. Esquinazi, J. Barzola-Quiquia, and S. Dusari, New J. Phys. **14**, 053015 (2012).

[3] B. T. Kelly, *Physics of Graphite* (Applied Science Publishers, London, 1981).

[4] Q. Lin, T. Li, Z. Liu, Y. Song, L. He, Z. Hu, Q. Guo, and H. Ye, Carbon **50**, 2369 (2012).

[5] C. E. Precker, P. D. Esquinazi, A. Champi, J. Barzola-Quiquia, M. Zoraghi, S. Muiños-Landin, A. Setzer, W. Böhlmann, D. Spemann, J. Meijer, T. Muenster, O. Baehre, G. Kloess, and H. Beth, New J. Phys. **18**, 113041 (2016).

[6] J. Barzola-Quiquia, J.-L. Yao, P. Rödiger, K. Schindler, and P. Esquinazi, Phys. Stat. Sol. (a) **205**, 2924 (2008).

[7] A. Ballestar, J. Barzola-Quiquia, T. Scheike, and P. Esquinazi, New J. Phys. **15**, 023024 (2013).

[8] T. Scheike, P. Esquinazi, A. Setzer, and W. Böhlmann, Carbon **59**, 140 (2013).

[9] A. Ballestar, P. Esquinazi, and W. Böhlmann, Phys. Rev. B **91**, 014502 (2015).

[10] P. D. Esquinazi and Y. Lysogorskiy, *Experimental Evidence for the Existence of Interfaces in Graphite and Their Relation to the Observed Metallic and Superconducting Behavior*, edited by P. Esquinazi (Springer International Publishing AG Switzerland, 2016), Chap. 7, pp. 145–179.

[11] M. Zoraghi, J. Barzola-Quiquia, M. Stiller, P. D. Esquinazi, and I. Estrela-Lopis, Carbon **139**, 1074 (2018).

[12] C. E. Precker, J. Barzola-Quiquia, P. D. Esquinazi, M. Stiller, M. K. Chan, M. Jaime, Z. Zhang, and M. Grundmann, Adv. Eng. Mater. **21**, 1970039 (2019).

[13] M. Kuwabara, D. R. Clarke, and A. A. Smith, Appl. Phys. Lett. **56**, 2396 (1990).

[14] M. Flores, E. Cisternas, J. Correa, and P. Vargas, Chem. Phys. **423**, 49 (2013).

[15] D. L. Miller, K. D. Kubista, G. M. Rutter, M. Ruan, W. A. de Heer, P. N. First, and J. A. Stroscio, Phys. Rev. B **81**, 125427 (2010).

[16] I. Brihuega, P. Mallet, H. González-Herrero, G. Trambly de Laissardière, M. M. Ugeda, L. Magaud, J. M. Gómez-Rodríguez, F. Ynduráin, and J.-Y. Veuillen, Phys. Rev. Lett. **109**, 196802 (2012).

[17] Y. Lu, M. Muñoz, C. S. Steplecaru, C. Hao, M. Bai, N. García, K. Schindler, and P. Esquinazi, Phys. Rev. Lett. **97**, 076805 (2006); see also the comment by S. Sadewasser and Th. Glatzel, *ibid.* **98**, 269701 (2007); and the reply by Lu *et al.*, *ibid.* **98**, 269702 (2007); and also R. Proksch, Appl. Phys. Lett. **89**, 113121 (2006).

[18] J. W. McClure, Phys. Rev. **104**, 666 (1956).

[19] B. Semenenko and P. Esquinazi, Magnetochemistry **4**, 52 (2018).

[20] J. W. McClure, Phys. Rev. **108**, 612 (1957).

[21] J. C. Slonczewski and P. R. Weiss, Phys. Rev. **109**, 272 (1958).

[22] J. W. McClure, Phys. Rev. **112**, 715 (1958).

[23] Y. Cao, V. Fatemi, S. Fang, K. Watanabe, T. Taniguchi, E. Kaxiras, and P. Jarillo-Herrero, Nature (London) **556**, 43 (2018).

[24] D. Marchenko, D. V. Evtushinsky, E. Golias, A. Varykhalov, Th. Seyller, and O. Rader, Sci. Adv. **4**, eaau0059 (2018).

[25] A. Ballestar, T. T. Heikkilä, and P. Esquinazi, Supercond. Sci. Technol. **27**, 115014 (2014).

[26] P. D. Esquinazi, C. E. Precker, M. Stiller, T. R. S. Cordeiro, J. Barzola-Quiquia, A. Setzer, and W. Böhlmann, Quantum Stud.: Math. Found. **5**, 41 (2018).

[27] M. Zoraghi, J. Barzola-Quiquia, M. Stiller, A. Setzer, P. Esquinazi, G. H. Kloess, T. Muenster, T. Lühmann, and I. Estrela-Lopis, Phys. Rev. B **95**, 045308 (2017).

[28] J. Barzola-Quiquia, P. D. Esquinazi, C. E. Precker, M. Stiller, M. Zoraghi, T. Förster, T. Herrmannsdörfer, and W. A. Coniglio, Phys. Rev. Materials **3**, 054603 (2019).

[29] G. H. Kinchin, Proc. R. Soc. Lond. A **217**, 9 (1953).

[30] S. Mrozowski and A. Chaberski, Phys. Rev. **104**, 74 (1956).

[31] D. E. Soule, Phys. Rev. **112**, 698 (1958).

[32] J. D. Cooper, J. Woore, and D. A. Young, Nature **225**, 721 (1970).

[33] N. B. Brandt, G. A. Kapustin, V. G. Karavaev, A. S. Kotosonov, and E. A. Svistova, Sov. Phys.-JETP **40**, 564 (1975).

[34] H. Oshima, K. Kawamura, T. Tsuzuku, and K. Sugihara, J Phys. Soc. Japan **51**, 1476 (1982).

[35] J. S. Bunch, Y. Yaish, M. Brink, K. Bolotin, and P. L. McEuen, Nano Lett. **5**, 287 (2005).

[36] R. Vansweevelt, V. Mortet, J. D'Haen, B. Ruttens, C. V. Haesendonck, B. Partoens, F. M. Peeters, and P. Wagner, Phys. Stat. Solidi A **208**, 1252 (2011).

[37] Y. Kopelevich, J. H. S. Torres, R. R. da Silva, F. Mrowka, H. Kempa, and P. Esquinazi, Phys. Rev. Lett. **90**, 156402 (2003).

[38] H. Kempa, P. Esquinazi, and Y. Kopelevich, Solid State Commun. **138**, 118 (2006).

[39] Y. Kopelevich, J. M. Pantoja, R. da Silva, F. Mrowka, and P. Esquinazi, Phys. Lett. A **355**, 233 (2006).

[40] J. M. Schneider, M. Orlita, M. Potemski, and D. K. Maude, Phys. Rev. Lett. **102**, 166403 (2009); see also the comment by I. A. Luk'yanchuk and Y. Kopelevich, *ibid.* **104**, 119701 (2010).

[41] P. Esquinazi, J. Krüger, J. Barzola-Quiquia, R. Schönemann, T. Hermannsdörfer, and N. García, AIP Adv. **4**, 117121 (2014).

[42] M. Breusing, C. Ropers, and T. Elsaesser, Phys. Rev. Lett. **102**, 086809 (2009).

[43] K. Sugawara, T. Sato, S. Souma, T. Takahashi, and H. Suematsu, Phys. Rev. Lett. **98**, 036801 (2007).

[44] A. Grüneis, C. Attaccalite, T. Pichler, V. Zabolotnyy, H. Shiozawa, S. L. Molodtsov, D. Inosov, A. Koitzsch, M. Knupfer, J. Schiessling, R. Follath, R. Weber, P. Rudolf, L. Wirtz, and A. Rubio, Phys. Rev. Lett. **100**, 037601 (2008).

[45] Y. Liu, L. Zhang, M. K. Brinkley, G. Bian, T. Miller, and T.-C. Chiang, Phys. Rev. Lett. **105**, 136804 (2010).

[46] R. Yin, Y. Zheng, X. Ma, Q. Liao, C. Ma, and B. Wang, Phys. Rev. B **102**, 115410 (2020).

[47] J. C. González, M. Muñoz, N. García, J. Barzola-Quiquia, D. Spoddig, K. Schindler, and P. Esquinazi, Phys. Rev. Lett. **99**, 216601 (2007).

[48] H. Henck, J. Avila, Z. Ben Aziza, D. Pierucci, J. Baima, B. Pamuk, J. Chaste, D. Utt, M. Bartos, K. Nogajewski, B. A. Piot, M. Orlita, M. Potemski, M. Calandra, M. C. Asensio, F. Mauri, C. Faugeras, and A. Ouerghi, Phys. Rev. B **97**, 245421 (2018).

[49] C. Li, S. Minne, B. Pittenger, and A. Mednick, *Simultaneous Electrical and Mechanical Property Mapping at the Nanoscale with PeakForce TUNA* (Bruker Nano Surfaces Division, Santa Barbara, CA, 2011), Bruker Application Note #132.

[50] D. Pierucci, H. Sediri, M. Hajlaoui, J.-C. Girard, T. Brumme, M. Calandra, E. Velez-Fort, G. Patriarche, M. G. Silly, G. Ferro, V. Souliere, M. Marangolo, F. Sirotti, F. Mauri, and A. Ouerghi, ACS Nano **9**, 5432 (2015).

[51] N. B. Kopnin, M. Ijäs, A. Harju, and T. T. Heikkilä, Phys. Rev. B **87**, 140503(R) (2013).

[52] G. E. Volovik, JETP Lett. **107**, 516 (2018).

[53] C. Cong, T. Yu, K. Sato, J. Shang, R. Saito, G. F. Dresselhaus, and M. S. Dresselhaus, ACS Nano **5**, 8760 (2011).

[54] Y. Henni, H. P. O. Collado, K. Nogajewski, M. R. Molas, G. Usaj, C. A. Balseiro, M. Orlita, M. Potemski, and C. Faugeras, Nano Lett. **16**, 3710 (2016).

[55] A. Torche, F. Mauri, J.-C. Charlier, and M. Calandra, Phys. Rev. Materials **1**, 041001(R) (2017).

[56] S. L. L. M. Ramos, M. A. Pimenta, and A. Champi, Carbon (2021), doi: 10.1016/j.carbon.2021.01.154.

[57] N. Agrait, J. Rodrigo, and S. Vieira, Ultramicroscopy **42-44**, 177 (1992).

[58] M. Schnedler, V. Portz, P. H. Weidlich, R. E. Dunin-Borkowski, and Ph. Ebert, Phys. Rev. B **91**, 235305 (2015).

[59] M. Schnedler, R. E. Dunin-Borkowski, and Ph. Ebert, Phys. Rev. B **93**, 195444 (2016).

[60] F. Rozplocha, J. Patyk, and J. Stankowski, Acta Phys. Pol. A **112**, 557 (2007).

[61] S. Dusari, J. Barzola-Quiquia, P. Esquinazi, and N. García, Phys. Rev. B **83**, 125402 (2011).

[62] A. Arndt, D. Spoddig, P. Esquinazi, J. Barzola-Quiquia, S. Dusari, and T. Butz, Phys. Rev. B **80**, 195402 (2009).

[63] M. Kaack and D. Fick, Surf. Sci. **342**, 111 (1995).

[64] K. S. Krishnan and S. C. Jain, Nature (London) **169**, 702 (1952).

[65] E. Rut'kov, E. Afanas'eva, and N. Gall, Diam. Relat. Mater. **101**, 107576 (2020).

[66] J. Bonoand R. H. Good, Surf. Sci. **175**, 415 (1986).

[67] R. M. Feenstra and J. A. Stroscio, J. Vac. Sci. Technol. B **5**, 923 (1987).

[68] W. A. Muñoz, L. Covaci, and F. M. Peeters, Phys. Rev. B **87**, 134509 (2013).

[69] R. Xu, L.-J. Yin, J.-B. Qiao, K.-K. Bai, J.-C. Nie, and L. He, Phys. Rev. B **91**, 035410 (2015).

[70] W. Wang, Y. Shi, A. A. Zakharov, M. Syväjärvi, R. Yakimova, R. I. G. Uhrberg, and J. Sun, Nano Lett. **18**, 5862 (2018).

[71] T. Heikkilä and G. E. Volovik, *Flat Bands as a Route to High-Temperature Superconductivity in Graphite*, edited by P. Esquinazi (Springer International Publishing AG Switzerland, 2016), pp. 123–144.

[72] B. Pamuk, J. Baima, F. Mauri, and M. Calandra, Phys. Rev. B **95**, 075422 (2017).

[73] R. Ojajärvi, T. Hyart, M. A. Silaev, and T. T. Heikkilä, Phys. Rev. B **98**, 054515 (2018).

[74] T. Hyart, R. Ojajärvi, and T. Heikkilä, J. Low Temp Phys **191**, 35 (2018).

[75] M. Schnedler, V. Portz, H. Eisele, R. E. Dunin-Borkowski, and Ph. Ebert, Phys. Rev. B **91**, 205309 (2015).

[76] V. Portz, M. Schnedler, L. Lymperakis, J. Neugebauer, H. Eisele, J.-F. Carlin, R. Butté, N. Grandjean, R. E. Dunin-Borkowski, and P. Ebert, Appl. Phys. Lett. **110**, 022104 (2017).

[77] D. Spemann and P. Esquinazi, *Evidence for Magnetic Order in Graphite from Magnetization and Transport Measurements*, edited by P. Esquinazi (Springer International Publishing AG Switzerland, 2016), pp. 45–76.